

# Scattering theory of thermal and bipolar thermoelectric diodes

José Balduque<sup>1,2</sup> and Rafael Sánchez<sup>1,2,3</sup>

<sup>1</sup>*Departamento de Física Teórica de la Materia Condensada, Universidad Autónoma de Madrid, 28049 Madrid, Spain*

<sup>2</sup>*Condensed Matter Physics Center (IFIMAC), Universidad Autónoma de Madrid, 28049 Madrid, Spain*

<sup>3</sup>*Instituto Nicolás Cabrera (INC), Universidad Autónoma de Madrid, 28049 Madrid, Spain*

(Dated: March 10, 2025)

We investigate the minimal requirements that induce a nonreciprocal response to temperature differences in a mesoscopic electronic conductor. We identify two distinct mechanisms due to electron-electron interactions, namely inelastic scattering and screening, to locally affect the internal properties of the device, leading to thermal and thermoelectric rectification effects in the absence of inversion symmetry. We propose resonant tunneling samples to efficiently exploit these effects, and find configurations acting as bipolar thermoelectric diodes whose current flows in the same direction irrespective of the sign of the temperature difference, a case of antireciprocity.

*Introduction.*—Macroscopic materials and devices typically show a linear response to temperature differences [1], with deviations being described recently in extended low-dimensional systems [2–4]. This regime is governed by the principle of microreversibility that has profound consequences such as Onsager reciprocity relations [5]. This means that reversing the temperature differences applied to the two terminals of a conductor changes the sign of the charge and heat currents, but not their magnitude. In the quantum regime, and in the absence of strong interactions, these properties can be derived from the scattering matrix defining the conductor close to equilibrium [6]. Nanoscale devices [7] which avoid these constraints are strongly demanded to define diodes whose conduction properties are sensitive to nonequilibrium states onchip (due to e.g., undesired hotspots or leakage heat flows): nonreciprocal currents are different in the forward (F) and backward (B) configurations, when a temperature increase  $\Delta T$  holds either on the left or on the right terminal, see Fig. 1(a). Most proposals so far are based on specific realizations dominated by electron-electron interactions [8–15], with so far very few experiments detecting nonreciprocal thermal or thermoelectric responses to temperature differences [16–18]. Some other works can be interpreted in terms of noninteracting electrons, however requiring the coupling to additional degrees of freedom (phonons, photons) [19–27], a quantum detector [28, 29] or a third terminal [15, 30–34], all involving heat being dissipated elsewhere, rather than rectified. Photonic thermal rectification in quantum information systems is also intensively investigated [35–46]. However, an overall description of the microscopic origin of temperature-driven electronic diodes is missing which is not restricted to near equilibrium situations [47–51].

Here we investigate the onset of temperature-driven diode effects by exploring the geometric and dynamic consequences of reduced dimensionality conductors: on one hand, they have a low capacitance [52]; on the other hand, their size can be comparable to the carrier thermalization length [53]. Both features emphasize the importance of electron-electron interactions: charge accumulation in the conductor alters the internal potential,

while the momentum transfer involved in the Coulomb interaction results in inelastic scattering, phase randomization and thermalization within the nanostructure. Importantly, we will not require any external environment, such that energy is conserved in the conductor: at low temperatures, the electron-phonon coupling is negligible. The key aspect is that the state of the quantum system is sensitive to the temperature distribution in the two terminals, for which one additionally needs to impose (left-right) inversion symmetry breaking.

To keep the discussion simple, we use a scattering theory based description, which is well established close to the linear regime as long as electron-electron interactions can be treated in a mean field level [54–56]. Nontrivial extensions of the theory are needed that account for nonlinearities [57] (relating charge accumulation in the conductor to rectification and diode effects [56]) and inelastic scattering [58–60] (treated phenomenologically). For this, we consider the configuration sketched in Fig. 1(a): thermoelectric particle,  $I$ , and heat,  $J$ , currents through

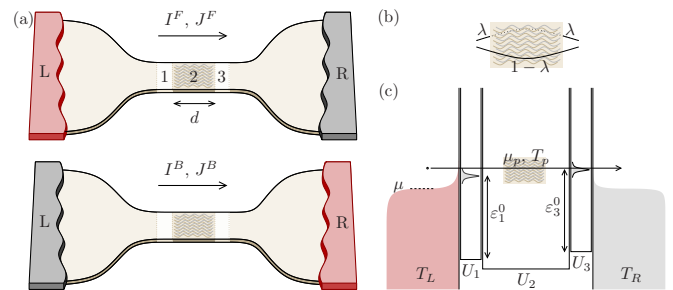


FIG. 1. Scheme of a temperature-induced diode. (a) It consists on three regions: 1 and 3, where transport is elastic, and 2, where electrons may thermalize. Particle ( $I$ ) and heat ( $J$ ) currents responding to differences in the temperature  $T_j$  of terminals  $j = L, R$  are sensitive to the forward (F) or backward (B) configuration where temperature is increased in terminal L or R. (b) Scheme of a probe modelling thermalization in region 2 which absorbs (reflects) electrons with probability  $\lambda$  ( $1-\lambda$ ), and (c) of a configuration where regions 1 and 2 are tunnel junctions with resonances at energy  $\epsilon_\alpha^0$  with respect to the corresponding band bottom,  $U_\alpha$ .

a quantum conductor are due to temperature differences between terminals L and R [61, 62]. The conductor is partitioned in three, with regions  $\alpha = 1, 3$  sandwiching region 2, of length  $d$ , where electrons are ballistic but have a finite probability  $\lambda$  to thermalize. Despite its simplicity, this model can be applied to a wide range of configurations, including quantum wires [63–67], molecular junctions [68, 69], chaotic cavities [70] (which enhance thermalization [71]) or quantum dots [72]. Remarkably, it not only allows us to identify the relevant mechanisms for thermoelectric and thermal rectification, it also predicts an antireciprocal response: a bipolar thermoelectric effect in particular configurations for which particles flow in the same direction independently of which terminal is hot. We discuss how this effect depends on the breaking of the microreversibility principle for the different involved mechanisms.

*Scattering theory.*— The transport properties of a single-channel conductor are described by its scattering matrix,  $\mathcal{S}(E)$ . With the current density in terminal  $j$

$$\mathcal{I}_j(E) = \frac{2}{h} \sum_k |\mathcal{S}_{kj}(E)|^2 [f_j(E) - f_k(E)] \quad (1)$$

one writes the particle,  $I_j = \int dE \mathcal{I}_j(E)$ , and heat currents,  $J_j = \int dE (E - \mu_j) \mathcal{I}_j(E)$  [61], where  $f_j(E) = 1/\{1 + \exp[(E - \mu_j)/k_B T_j]\}$  is the Fermi function of terminal  $j$  at temperature  $T_j$  and electrochemical potential  $\mu_j$ ,  $h$  and  $k_B$  are the Planck and Boltzmann constants, and the factor 2 accounts for spin degeneracy [73]. We consider the scattering region to have a piecewise uniform band bottom  $\mathbf{U} \equiv \{U_\alpha\}$ , which will influence the shape of  $\mathcal{S}(E) = \mathcal{S}(E, \mathbf{U})$ . For later convenience, we split them into equilibrium (including the effect of gate voltages) and nonequilibrium contributions:  $U_\alpha = U_\alpha^{\text{eq}} + U_\alpha^{\text{neq}}$ . Note that since the particle flow relies on the thermoelectric effect,  $\mathcal{S}(E)$  needs to be energy dependent [53].

We are interested in two-terminal conductors, with  $j = L, R$ , only driven by a temperature difference  $\Delta T$  applied either to L (the forward) or to R (the backward case), with the opposite terminal being at temperature  $T$ , and both having the same electrochemical potential,  $\mu = \mu_L = \mu_R$ . The diode effect appears when the particle or heat currents,  $X^i(T_L, T_R) = I_L^i, J_L^i$  ( $i = F, B$ ), are nonreciprocal i.e.,  $X^F \neq -X^B$ , with  $X^F \equiv X(T + \Delta T, T)$  and  $X^B \equiv X(T, T + \Delta T)$ . We quantify this effect with the thermoelectric,  $\mathcal{R}_I$ , and thermal,  $\mathcal{R}_J$ , rectification coefficients [74]

$$\mathcal{R}_X = \frac{X^F + X^B}{|X^F| + |X^B|}, \quad (2)$$

which saturate to  $\pm 1$  only when one of the currents is zero (perfect diode) or when both have the same sign. In the latest case, the diode is bipolar.

We readily see that assuming fully-noninteracting particles, for which the scattering matrix is independent of the reservoir temperatures, both currents  $X^i$  are anti-symmetric under the exchange  $T_L \leftrightarrow T_R$ , c.f. Eq. (1) for

$j = L$  and  $k = R$ , resulting in no rectification,  $\mathcal{R}_X = 0$ . A diode hence needs that the nanostructure is sensitive to the terminal temperatures.

In what follows, we explore the role of interactions as a requisite for thermal and thermoelectric rectification. We consider two separate ways in which interactions can modify the electron propagation through the system, namely inelastic scattering and screening effects.

*Inelastic scattering.*— When two electrons interact, they exchange momentum, involving that they change their energies and randomize their kinetic phases, limiting both the elastic and phase-coherent transport implicit in Eq. (1), while conserving their total energy. In scattering theory, this effect is routinely described phenomenologically by introducing a fictitious probe [59, 60, 75–79] which absorbs electrons with probability  $\lambda$  [80] and reinjects them with a random phase and thermalized with a distribution  $f_p(E)$  whose electrochemical potential,  $\mu_p$ , and temperature,  $T_p$ , are determined by imposing that the probe injects no particle and no heat currents on average,  $I_p = J_p = 0$ . Intuitively  $\lambda$  relates the inelastic scattering length  $l_{\text{inel}}$  to the typical size of the system,  $l$ :  $\lambda \ll 1$  when  $l_{\text{inel}} \gg l$ , and  $\lambda \approx 1$  in the opposite limit. Quantum Hall realizations relate  $\lambda$  to the transmission of a quantum point contact [81]. Trajectories involving the probe do not obey microreversibility. On a microscopic description of the particular models, there may be small deviations from a Fermi distribution function, specially at very low temperatures and far from equilibrium [82] which are not relevant for our discussion here. Our thermalization probe, sketched in Fig. 1(b), is hence formally equivalent to a thermometer [83–86] and useful to discuss thermalization in hot-carrier solar cells [87], broken-time-reversal-induced electrical diodes [78] and correlations in edge channels [88]. Note that while the flow of heat will be determined by  $T_L - T_R$ , the particle currents may be affected by the competition of the thermoelectric effect and the developed  $\mu_p - \mu$ .

The rectification properties of thermalization is proven analytically by considering a simple configuration in which all electrons in the conductor are thermalized ( $\lambda = 1$ ), with region 3 being transparent (so  $\mathcal{S}_{pR} = 1$ ) and region 1 being a barrier with transmission probability  $\mathcal{T}(E) = |\mathcal{S}_{pL}(E)|^2$ , c.f. Fig. 1(a). In the limit  $\mu - U_\alpha \gg k_B T$ , the contribution of terminal R to the currents into the probe are given by  $\int dE [f_R(E) - f_p(E)] = \mu - \mu_p$  and  $\int dE E [f_R(E) - f_p(E)] = \pi^2 (T_R^2 - T_p^2)/6$ . The other contribution to the probe currents coincides with  $X^i$ , which are then determined by the probe conditions:

$$I^i = \frac{2}{h} (\mu_{p,i} - \mu) \quad \text{and} \quad J^i = \frac{\pi^2}{3h} (T_{p,i}^2 - T_{R,i}^2), \quad (3)$$

with  $T_{R,F} = T$  and  $T_{R,B} = T + \Delta T$ . The spatial asymmetry here is due to the position of the thermalization region with respect to the thermoelectric element, which is enough to have  $T_p^F \neq T_p^B$ . A thermoelectric diode needs that  $\mathcal{T}(E)$  breaks electron-hole symmetry, so region 1 has a finite electric response giving  $\mu_p^F \neq \mu_p^B$  [80].

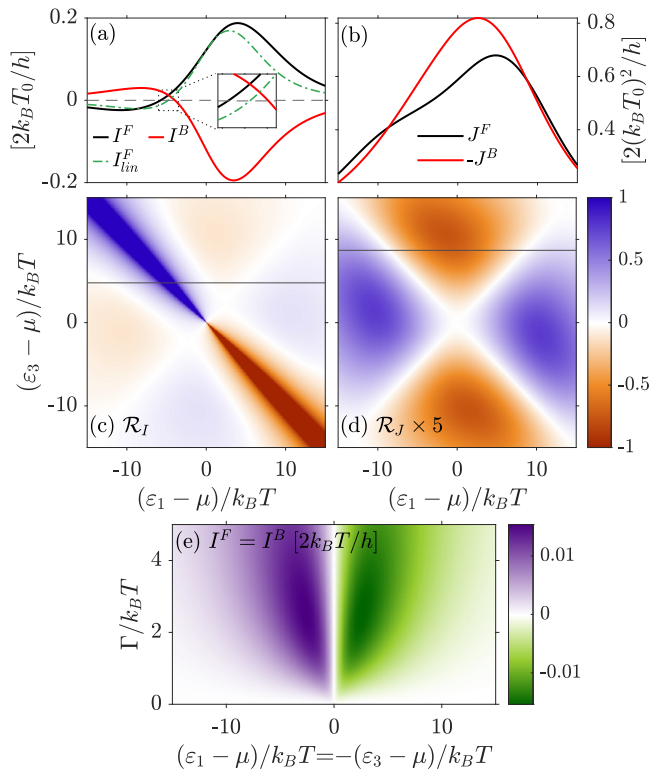


FIG. 2. Thermalization diode. Forward and backward (a) particle and (b) heat currents as functions of  $\varepsilon_1$  tuned along  $(\varepsilon_3 - \mu)/k_B T = 4.8$  and  $8.7$ , respectively, indicated by black lines in (c) and (d). The later panels show the thermoelectric and heat rectification coefficients, as functions of both resonances. The thermalization probe is fully coupled ( $\lambda = 1$ ), and  $\mu \gg U_\alpha$ , avoiding band bottom effects. The linear response current,  $I_{lin}^F = L^{(1)F} \Delta T$ , is shown for comparison in (a). Parameters:  $\Gamma = 3k_B T$ ,  $\mu = 40k_B T$  and  $\Delta T/T = 1$ .

We now consider a more specific setup, sketched in Fig. 1(c), which allows us to control the degree of asymmetry experimentally [72, 89]. We choose the scattering regions 1 and 3 to be resonant-tunneling barriers (RTB), known efficient thermoelectric devices [90–94]. We model them by Breit-Wigner resonances [95] with energy  $\varepsilon_\alpha^0$  and inverse lifetime  $\Gamma_\alpha/\hbar$  [60] and transmission amplitude [80]

$$\tau_\alpha = \frac{-i\Gamma_\alpha}{E - \varepsilon_\alpha^0 - U_\alpha + i\Gamma_\alpha}, \quad (\alpha=1,3). \quad (4)$$

For simplicity, we assume  $\Gamma_1 = \Gamma_3 = \Gamma$ , and a totally-coupled probe so direct elastic transport between terminals L and R is suppressed, a configuration of experimental relevance [72, 96, 97]. We incorporate  $U_\alpha^{eq}$ , which allows us to control the system asymmetry via gate voltages, in the resonance energies  $\varepsilon_\alpha = \varepsilon_\alpha^0 + U_\alpha^{eq}$ , and neglect  $U_\alpha^{neq}$  here.

The resulting currents and rectification coefficients are plotted in Figs. 2(a)-(d) by tuning the resonance energies of the barriers. As expected, broken inversion symmetry when  $\varepsilon_1 \neq \varepsilon_3$  results in finite  $\mathcal{R}_I$  and  $\mathcal{R}_J$ , while  $\mathcal{R}_I = 0$  for symmetric cases with  $\varepsilon_1 = \varepsilon_3$ .

The antisymmetric configuration with  $\varepsilon_1 - \mu = \mu - \varepsilon_3$  is particularly interesting: while inversion symmetry is maximally broken, it respects electron-hole symmetry in equilibrium. The two RTB have opposite thermoelectric contributions resulting in a vanishing linear response for particles, see Fig. 2(a): writing  $I^i = \sum_n L^{(n),i} \Delta T^n$ , we get  $L^{(1),i} = 0$ , with the probe developing a temperature  $T_p^F = T_p^B = T + \Delta T/2$  and electrochemical potentials of opposite sign in F and B,  $\mu_p^F + \mu_p^B = 2\mu$  [80]. This affects the nonlinear terms (of order  $\geq \Delta T^2$ ), making  $I^F$  and  $I^B$  vanish at different points (determined by the corresponding  $\mu_p$  and  $T_p$ ) when, e.g., tuning  $\varepsilon_1$ , see inset in Fig. 2(a). At the vanishing points, the current flows only in one of the configurations, as an ideal thermoelectric diode with  $\mathcal{R}_I = 1$  (however working only for a particular  $\Delta T$ ). Most remarkably, between them, the current flows in the same direction irrespectively of which terminal is hot. This is what we call a bipolar thermoelectric (or antireciprocal) diode. Furthermore, at the antisymmetric condition  $\varepsilon_1 + \varepsilon_3 = 2\mu$ , the problem symmetry imposes  $I^F = I^B$  [80], with their sign being tunable and maximal for widths  $\Gamma \approx 2k_B T$  (consistent with similar configurations [98–100]), see Fig. 2(e).

Differently, the heat currents do not change sign (as imposed by the second law), see Fig. 2(b), which avoids a bipolar thermal diode if  $\mu_j = \mu$ . We find  $\mathcal{R}_J \sim 15\%$ , cf. Fig. 2(d), and  $\mathcal{R}_J = 0$  for  $(\varepsilon_1 - \mu) = \pm(\varepsilon_3 - \mu)$ , where both RTBs conduct heat equally.

*Screening effects.*— The injection of a charge current is able to alter the potential landscape of the conductor via charge accumulation and screening effects in the nearby gates defining the scattering regions [101, 102]. This consequence of electron-electron interaction is in fact needed to ensure gauge invariance in nonlinear scenarios [57]. Deviations from the linear regime leading to finite thermal and thermoelectric rectification have been discussed in the weakly interacting regime [47, 49–51].

We again test this mechanism in the setup of Fig. 1(c), now with  $\lambda = 0$ , so that transport between terminals is fully elastic. Then, an important contribution will be the internal reflections in region 2, leading to Fabry-Perot interferences. Scattering at the barriers is again given by Eq. (S3). Screening affects the internal electrostatic energies,  $\mathbf{U}$ , by developing finite  $U_\alpha^{neq}(T_L, T_R)$ , and modifies the scattering matrix of the whole system,  $\mathcal{S}(E, \mathbf{U})$  [80]. The energies  $\mathbf{U}$  are linked by

$$\delta q_\alpha = \sum_{\beta=1,2,3 \neq \alpha} C_{\alpha\beta} (U_\beta - U_\alpha) / (-e), \quad (5)$$

where  $\delta q_\alpha$  is the injected charge in region  $\alpha$  with respect to the equilibrium scenario, and  $C_{\alpha\beta}$  the geometric capacitance between regions  $\alpha$  and  $\beta$ , treated here as a parameter. The excess charge can be calculated with the aid of the partial local densities of states of the system, or injectivities [102],

$$\nu_{j\alpha}(E, \mathbf{U}) = \frac{i}{4\pi} \sum_k \left[ \mathcal{S}_{kj}^\dagger \frac{\delta \mathcal{S}_{kj}}{\delta U_\alpha} - \frac{\delta \mathcal{S}_{kj}^\dagger}{\delta U_\alpha} \mathcal{S}_{kj} \right], \quad (6)$$

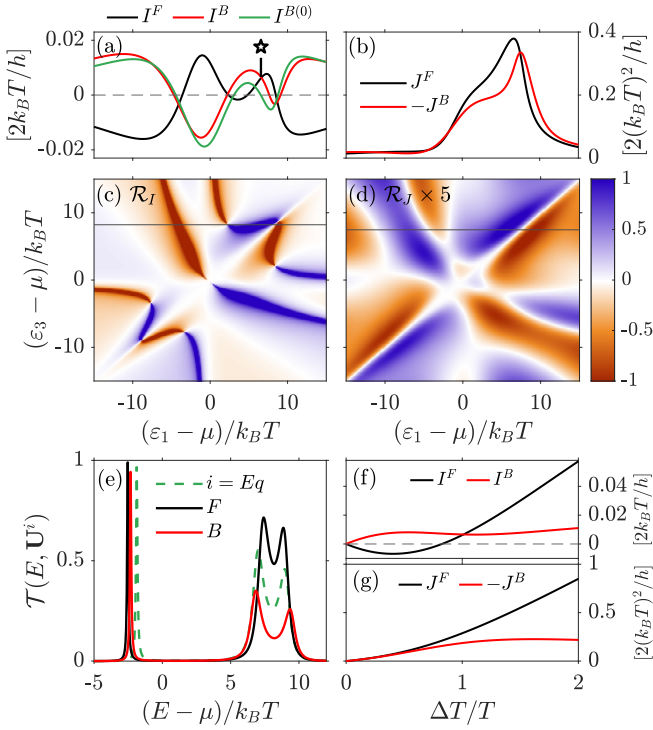


FIG. 3. Rectification by screening. (a) Particle and (b) heat currents as functions of  $\varepsilon_1$ , for fixed  $(\varepsilon_3 - \mu)/k_B T = 8.2$  and  $7.5$  as marked by black lines in (c) and (d), respectively. The later show the dependence of  $\mathcal{R}_I$  and  $\mathcal{R}_J$  with gating the RTBs. The green curve in (a) shows the current obtained by imposing the equilibrium transmission probability, for comparison. (e) Transmission probability in equilibrium and in the F and B configurations at the point marked by  $\star$  in (a), for which the temperature dependence of the charge and heat currents are shown in (f) and (g). Parameters:  $\lambda=0$ ,  $d = 2h/\sqrt{8mk_B T}$ ,  $\Gamma = k_B T$ ,  $\mu = 40k_B T$ ,  $\Delta T/T = 1$ .

defining the overlap of waves in region  $\alpha$  with states injected at terminal  $j$ , via

$$\frac{\delta q_\alpha}{-e} = \int dE \sum_j [\nu_{j\alpha}(E, \mathbf{U}) f_j(E) - \nu_{j\alpha}^{\text{eq}} f_{\text{eq}}(E)], \quad (7)$$

with  $\nu_{j\alpha}^{\text{eq}}$  and  $f_{\text{eq}}(E)$  evaluated at equilibrium. Note that we do not assume a weak deviation from equilibrium [103].

We show in Figs. 3(a) and 3(b) the resulting currents in the limit  $C_{\alpha\beta} \rightarrow 0$  for small conductors. The thermoelectric response shows an oscillating behaviour, with sign changes close to the crossings of the barrier resonances by the chemical potential, and at the crossing of the two resonances. As  $\mathbf{U}$  depends on the temperature distribution, these crossings occur at different points in F and B, again resulting in regions with  $\mathcal{R}_I = 1$ , see Fig. 3(c). The heat currents do not change sign, finding wide regions with strong rectification ( $\mathcal{R}_J \sim 0.2$ ) close to the resonance condition  $\varepsilon_1 \approx \varepsilon_3$ , see Fig. 3(d).

Screening hence also induces a bipolar thermoelectric diode, in this case respecting microreversibility:

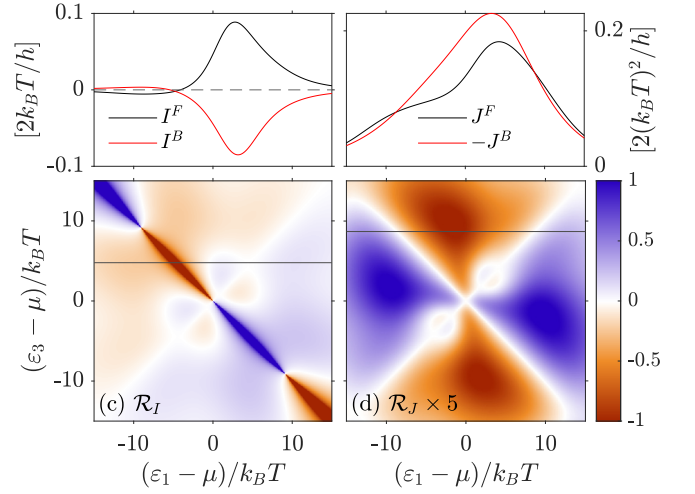


FIG. 4. Mixed configuration. Same as Figs. 3(a)-(d) for  $\lambda=1$ .

$|\mathcal{S}_{LR}(E, \mathbf{U})|^2 = |\mathcal{S}_{RL}(E, \mathbf{U})|^2 = \mathcal{T}(E)$ . To further understand this mechanism, let us concentrate on the particular configuration marked by  $\star$  in Fig. 3(a), where  $I^F = I^B$ . There, both resonances are over the chemical potential and slightly detuned,  $\varepsilon_3 > \varepsilon_1 > \mu$ . The transmission probability  $\mathcal{T}(E)$  [see Fig. 3(e)] shows two main features with opposite thermoelectric contributions: a wide double peak around  $\varepsilon_1, \varepsilon_3 > \mu$ , and a sharp peak at  $E < \mu$  due to the Fabry-Perot interference in  $\alpha=2$ . Note that  $\mathcal{T}(E \approx \mu)$  is flat, which suppresses the linear term ( $L^{(1)} \propto \partial \mathcal{T} / \partial E$ ) according to the Mott formula [53]. In F, increasing  $T_L$  increases  $\delta q_1$  and hence  $U_1$ , bringing the two Breit-Wigner resonances closer and resulting in a sharper and higher double peak at positive energies, see Fig. 3(e). Oppositely, the corresponding increase of  $U_3$  in B separates the two resonances, making the double peak wider and lower, i.e., reducing its contribution to  $I^B$ . Eventually, the opposite contribution of the Fabry-Perot peak at negative energies dominates, inducing  $I^B$  to change sign [80]. This bipolar diode is hence induced not only by screening but also by quantum interference.

The bipolar effect persists for higher  $\Delta T$ , cf. Fig. 3(f), and the thermal diode is robust: one polarity exhibits vanishing and even negative thermal differential conductance for large  $\Delta T$  [80], see Fig. 3(g). We attribute this effect to the same mechanism discussed above.

*Mixed regime*.— To confirm the quantum interference origin of the screening-induced bipolar thermoelectric diode, we compute a mixed configuration where screening coexists with thermalization, cf. Fig. 4. For  $\lambda = 1$ , the probe avoids any Fabry-Perot interference in region 2. Hence screening only contributes to shift  $U_1$  and  $U_3$ . By comparing Figs. 2, 3 and 4 we see that the currents are indeed dominated by thermalization, and the interference-induced off-diagonal features in  $\mathcal{R}_I$  are strongly suppressed [80]. Still, we find a thermalization-induced bipolar effect around  $\varepsilon_1 - \mu = \mu - \varepsilon_3$ .

*Conclusions*.— We have provided a fully quantum me-

chanical description of temperature-induced mesoscopic diodes by considering interaction-induced thermalization and screening affecting elastic transport (however strongly correlated effects like Coulomb blockade are not covered [104]). With this we find diode effects both for particle and thermal currents. Remarkably, we find an *antireciprocal* response in the form of a bipolar thermoelectric effect caused by both thermalization and screening-controlled quantum interference in ballistic resonant tunneling configurations. While the fully thermalized case can be interpreted in terms of locally reversing currents between three regions (the reservoirs and the internal thermalization region) at different thermal configurations, the fully coherent case exploits nonequilibrium states and quantum interference to achieve antireciprocity while maintaining microreversibility. In both cases, it occurs when sharp spectral features with opposite but similar in magnitude thermoelectric contributions depend differently on the local reaction of the

conductor to the nonequilibrium situation. We find measurable currents of a few nA at mK temperatures in state of the art configurations [72, 97].

Related effects have been predicted before however requiring dissipation [25, 28, 29] or multiterminal configurations [31, 33, 34]. Differently, our treatment imposes particle and energy conservation in the two-terminal diode. Our results add to other recently found bipolar nonlinear thermoelectric functionalities in superconducting junctions [105–107] (based on spontaneous symmetry breaking mechanisms), contributing to set the base for thermally-driven onchip devices.

We thank Y. Tokura and A. Braggio for useful discussions. We acknowledge funding from the Spanish Ministerio de Ciencia e Innovación via grants No. PID2019-110125GB-I00 and No. PID2022-142911NB-I00, and through the “María de Maeztu” Programme for Units of Excellence in R&D CEX2023-001316-M.

- 
- [1] N. W. Ashcroft and N. D. Mermin, *Solid State Physics* (Saunders College Publishing, Orlando, US, 1976).
- [2] Y. Wang, Z.-G. Zhu, and G. Su, Quantum theory of nonlinear thermal response, *Phys. Rev. B* **106**, 035148 (2022).
- [3] T. Yamaguchi, K. Nakazawa, and A. Yamakage, Microscopic theory of nonlinear Hall effect induced by electric field and temperature gradient, *Phys. Rev. B* **109**, 205117 (2024).
- [4] H. Arisawa, Y. Fujimoto, T. Kikkawa, and E. Saitoh, Observation of nonlinear thermoelectric effect in MoGe/Y3Fe5O12, *Nat. Commun.* **15**, 6912 (2024).
- [5] L. Onsager, Reciprocal Relations in Irreversible Processes. I., *Phys. Rev.* **37**, 405 (1931); Reciprocal Relations in Irreversible Processes. II., *Phys. Rev.* **38**, 2265 (1931).
- [6] P. Jacquod, R. S. Whitney, J. Meair, and M. Büttiker, Onsager relations in coupled electric, thermoelectric, and spin transport: The tenfold way, *Phys. Rev. B* **86**, 155118 (2012).
- [7] J. P. Pekola and B. Karimi, Colloquium: Quantum heat transport in condensed matter systems, *Rev. Mod. Phys.* **93**, 041001 (2021).
- [8] C. Xue-Ou, D. Bing, and L. Xiao-Lin, Thermal Rectification Effect of an Interacting Quantum Dot, *Chin. Phys. Lett.* **25**, 3032 (2008).
- [9] D. M.-T. Kuo and Y.-c. Chang, Thermoelectric and thermal rectification properties of quantum dot junctions, *Phys. Rev. B* **81**, 205321 (2010).
- [10] T. Ruokola and T. Ojanen, Single-electron heat diode: Asymmetric heat transport between electronic reservoirs through Coulomb islands, *Phys. Rev. B* **83**, 241404 (2011).
- [11] M. A. Sierra and D. Sánchez, Strongly nonlinear thermovoltage and heat dissipation in interacting quantum dots, *Phys. Rev. B* **90**, 115313 (2014).
- [12] M. A. Sierra and D. Sánchez, Nonlinear Heat Conduction in Coulomb-blockaded Quantum Dots, *Mater. Today: Proc.* **2**, 483 (2015).
- [13] L. Vannucci, F. Ronetti, G. Dolcetto, M. Carrega, and M. Sasseti, Interference-induced thermoelectric switching and heat rectification in quantum Hall junctions, *Phys. Rev. B* **92**, 075446 (2015).
- [14] A. Marcos-Vicioso, C. López-Jurado, M. Ruiz-Garcia, and R. Sánchez, Thermal rectification with interacting electronic channels: Exploiting degeneracy, quantum superpositions, and interference, *Phys. Rev. B* **98**, 035414 (2018).
- [15] L. Tesser, B. Bhandari, P. A. Erdman, E. Paladino, R. Fazio, and F. Taddei, Heat rectification through single and coupled quantum dots, *New J. Phys.* **24**, 035001 (2022).
- [16] R. Scheibner, M. König, D. Reuter, A. D. Wieck, C. Gould, H. Buhmann, and L. W. Molenkamp, Quantum dot as thermal rectifier, *New J. Phys.* **10**, 083016 (2008).
- [17] S. F. Svensson, E. A. Hoffmann, N. Nakpathomkun, P. M. Wu, H. Q. Xu, H. A. Nilsson, D. Sánchez, V. Kashcheyevs, and H. Linke, Nonlinear thermovoltage and thermocurrent in quantum dots, *New J. Phys.* **15**, 105011 (2013).
- [18] J. Fast, H. Lundström, S. Dorsch, L. Samuelson, A. Burke, P. Samuelsson, and H. Linke, Geometric symmetry breaking and nonlinearity can increase thermoelectric power, *Phys. Rev. Lett.* **133**, 116302 (2024).
- [19] D. Segal, Single mode heat rectifier: Controlling energy flow between electronic conductors, *Phys. Rev. Lett.* **100**, 105901 (2008).
- [20] M. J. Martínez-Pérez and F. Giazotto, Efficient phase-tunable Josephson thermal rectifier, *Appl. Phys. Lett.* **102**, 182602 (2013).
- [21] M. J. Martínez-Pérez, A. Fornieri, and F. Giazotto, Rectification of electronic heat current by a hybrid thermal diode, *Nat. Nanotechnol.* **10**, 303 (2015).
- [22] J.-H. Jiang, M. Kulkarni, D. Segal, and Y. Imry, Phonon thermoelectric transistors and rectifiers, *Phys. Rev. B* **92**, 045309 (2015).
- [23] G. Rosselló, R. López, and R. Sánchez, Dynamical

- Coulomb blockade of thermal transport, *Phys. Rev. B* **95**, 235404 (2017).
- [24] G. T. Craven, D. He, and A. Nitzan, Electron-transfer-induced thermal and thermoelectric rectification, *Phys. Rev. Lett.* **121**, 247704 (2018).
- [25] J. Lu, R. Wang, J. Ren, M. Kulkarni, and J.-H. Jiang, Quantum-dot circuit-QED thermoelectric diodes and transistors, *Phys. Rev. B* **99**, 035129 (2019).
- [26] B. Cao, C. Han, X. Hao, C. Wang, and J. Lu, Impact of Quantum Coherence on Inelastic Thermoelectric Devices: From Diode to Transistor, *Chin. Phys. Lett.* **41**, 077302 (2024).
- [27] E. L. Mehring, R. A. Bustos-Marín, and H. L. Calvo, Hysteresis and effective reciprocity breaking due to current-induced forces, *Phys. Rev. B* **109**, 085418 (2024).
- [28] P. Bredol, H. Boschker, D. Braak, and J. Mannhart, Decoherence effects break reciprocity in matter transport, *Phys. Rev. B* **104**, 115413 (2021).
- [29] J. Ferreira, T. Jin, J. Mannhart, T. Giamarchi, and M. Filippone, Transport and nonreciprocity in monitored quantum devices: An exact study, *Phys. Rev. Lett.* **132**, 136301 (2024).
- [30] R. Sánchez, B. Sothmann, and A. N. Jordan, Heat diode and engine based on quantum Hall edge states, *New J. Phys.* **17**, 075006 (2015).
- [31] R. Sánchez, H. Thierschmann, and L. W. Molenkamp, Single-electron thermal devices coupled to a mesoscopic gate, *New J. Phys.* **19**, 113040 (2017).
- [32] D. Goury and R. Sánchez, Reversible thermal diode and energy harvester with a superconducting quantum interference single-electron transistor, *Appl. Phys. Lett.* **115**, 092601 (2019).
- [33] G. Fleury, C. Gorini, and R. Sánchez, Scanning probe-induced thermoelectrics in a quantum point contact, *Appl. Phys. Lett.* **119**, 043101 (2021).
- [34] R. Sánchez, C. Gorini, and G. Fleury, Extrinsic thermoelectric response of coherent conductors, *Phys. Rev. B* **104**, 115430 (2021).
- [35] D. Segal and A. Nitzan, Spin-boson thermal rectifier, *Phys. Rev. Lett.* **94**, 034301 (2005).
- [36] T. Ojanen, Selection-rule blockade and rectification in quantum heat transport, *Phys. Rev. B* **80**, 180301 (2009).
- [37] F. Fratini, E. Mascarenhas, L. Safari, J.-P. Poizat, D. Valente, A. Auffèves, D. Gerace, and M. F. Santos, Fabry-Perot Interferometer with Quantum Mirrors: Nonlinear Light Transport and Rectification, *Phys. Rev. Lett.* **113**, 243601 (2014).
- [38] G. Schaller, G. G. Giusteri, and G. L. Celardo, Collective couplings: Rectification and supertransmittance, *Phys. Rev. E* **94**, 032135 (2016).
- [39] J. Ordonez-Miranda, Y. Ezzahri, and K. Joulain, Quantum thermal diode based on two interacting spinlike systems under different excitations, *Phys. Rev. E* **95**, 022128 (2017).
- [40] S. Barzanjeh, M. Aquilina, and A. Xuereb, Manipulating the flow of thermal noise in quantum devices, *Phys. Rev. Lett.* **120**, 060601 (2018).
- [41] J. Senior, A. Gubaydullin, B. Karimi, J. T. Peltonen, J. Ankerhold, and J. P. Pekola, Heat rectification via a superconducting artificial atom, *Commun. Phys.* **3**, 40 (2020).
- [42] B. Bhandari, P. A. Erdman, R. Fazio, E. Paladino, and F. Taddei, Thermal rectification through a nonlinear quantum resonator, *Phys. Rev. B* **103**, 155434 (2021).
- [43] A. Iorio, E. Strambini, G. Haack, M. Campisi, and F. Giazotto, Photonic heat rectification in a system of coupled qubits, *Phys. Rev. Appl.* **15**, 054050 (2021).
- [44] R. Upadhyay, D. S. Golubev, Y.-C. Chang, G. Thomas, A. Guthrie, J. T. Peltonen, and J. P. Pekola, Microwave quantum diode, *Nat. Commun.* **15**, 630 (2024).
- [45] K. Poulsen and N. T. Zinner, Heat-based circuits using quantum rectification, *Phys. Rev. A* **109**, 052223 (2024).
- [46] A. L. Yeyati, D. Subero, J. P. Pekola, and R. Sánchez, Photonic heat transport through a Josephson junction in a resistive environment, *Phys. Rev. B* **110**, L220502 (2024).
- [47] D. Sánchez and R. López, Scattering Theory of Nonlinear Thermoelectric Transport, *Phys. Rev. Lett.* **110**, 026804 (2013).
- [48] R. S. Whitney, Nonlinear thermoelectricity in point contacts at pinch off: A catastrophe aids cooling, *Phys. Rev. B* **88**, 064302 (2013).
- [49] R. S. Whitney, Thermodynamic and quantum bounds on nonlinear dc thermoelectric transport, *Phys. Rev. B* **87**, 115404 (2013).
- [50] J. Meair and P. Jacquod, Scattering theory of nonlinear thermoelectricity in quantum coherent conductors, *J. Phys.: Condens. Matter* **25**, 082201 (2013).
- [51] R. López and D. Sánchez, Nonlinear heat transport in mesoscopic conductors: Rectification, Peltier effect, and Wiedemann-Franz law, *Phys. Rev. B* **88**, 045129 (2013).
- [52] T. Ihn, *Semiconductor Nanostructures: Quantum states and electronic transport* (Oxford University Press, 2009).
- [53] G. Benenti, G. Casati, K. Saito, and R. S. Whitney, Fundamental aspects of steady-state conversion of heat to work at the nanoscale, *Phys. Rep.* **694**, 1 (2017).
- [54] R. Landauer, Spatial Variation of Currents and Fields Due to Localized Scatterers in Metallic Conduction, *IBM J. Res. Dev.* **1**, 223 (1957).
- [55] R. Landauer, Conductance determined by transmission: probes and quantised constriction resistance, *J. Phys.: Condens. Matter* **1**, 8099 (1989).
- [56] M. Büttiker and T. Christen, Admittance and Nonlinear Transport in Quantum Wires, Point Contacts, and Resonant Tunneling Barriers, in *Mesoscopic Electron Transport* (Springer, Dordrecht, The Netherlands, 1997) pp. 259–289.
- [57] T. Christen and M. Büttiker, Gauge-invariant nonlinear electric transport in mesoscopic, *Europhys. Lett.* **35**, 523 (1996).
- [58] H.-L. Engquist and P. W. Anderson, Definition and measurement of the electrical and thermal resistances, *Phys. Rev. B* **24**, 1151(R) (1981).
- [59] M. Büttiker, Role of quantum coherence in series resistors, *Phys. Rev. B* **33**, 3020 (1986).
- [60] M. Büttiker, Coherent and sequential tunneling in series barriers, *IBM J. Res. Dev.* **32**, 63 (1988).
- [61] U. Sivan and Y. Imry, Multichannel Landauer formula for thermoelectric transport with application to thermopower near the mobility edge, *Phys. Rev. B* **33**, 551 (1986).
- [62] P. N. Butcher, Thermal and electrical transport formalism for electronic microstructures with many terminals, *J. Phys.: Condens. Matter* **2**, 4869 (1990).
- [63] P. Streda, Quantised thermopower of a channel in the

- ballistic regime, *J. Phys.: Condens. Matter* **1**, 1025 (1989).
- [64] L. W. Molenkamp, H. van Houten, C. W. J. Beenakker, R. Eppenga, and C. T. Foxon, Quantum oscillations in the transverse voltage of a channel in the nonlinear transport regime, *Phys. Rev. Lett.* **65**, 1052 (1990).
- [65] G. D. Guttman, E. Ben-Jacob, and D. J. Bergman, Thermopower of mesoscopic and disordered systems, *Phys. Rev. B* **51**, 17758 (1995).
- [66] S. Kheradsoud, N. Dashti, M. Misiorny, P. P. Potts, J. Splettstoesser, and P. Samuelsson, Power, Efficiency and Fluctuations in a Quantum Point Contact as Steady-State Thermoelectric Heat Engine, *Entropy* **21**, 777 (2019).
- [67] G. Haack and F. Giazotto, Efficient and tunable Aharonov-Bohm quantum heat engine, *Phys. Rev. B* **100**, 235442 (2019).
- [68] M. Paulsson and S. Datta, Thermoelectric effect in molecular electronics, *Phys. Rev. B* **67**, 241403 (2003).
- [69] P. Reddy, S.-Y. Jang, R. A. Segalman, and A. Majumdar, Thermoelectricity in molecular junctions, *Science* **315**, 1568 (2007).
- [70] D. Sánchez and L. Serra, Thermoelectric transport of mesoscopic conductors coupled to voltage and thermal probes, *Phys. Rev. B* **84**, 201307 (2011).
- [71] C. Rangi, H. F. Fotsos, H. Terletska, J. Moreno, and K.-M. Tam, Disorder Enhanced Thermalization in Interacting Many-Particle System, [arXiv:2405.13876](https://arxiv.org/abs/2405.13876) (2024).
- [72] G. Jaliel, R. K. Puddy, R. Sánchez, A. N. Jordan, B. Sothmann, I. Farrer, J. P. Griffiths, D. A. Ritchie, and C. G. Smith, Experimental realization of a quantum dot energy harvester, *Phys. Rev. Lett.* **123**, 117701 (2019).
- [73] T. T. Heikkilä, *The Physics of Nanoelectronics* (Oxford University Press, Oxford, England, UK, 2013).
- [74] S. Khandelwal, M. Perarnau-Llobet, S. Seah, N. Brunner, and G. Haack, Characterizing the performance of heat rectifiers, *Phys. Rev. Res.* **5**, 013129 (2023).
- [75] J. L. D'Amato and H. M. Pastawski, Conductance of a disordered linear chain including inelastic scattering events, *Phys. Rev. B* **41**, 7411 (1990).
- [76] M. J. M. de Jong and C. W. J. Beenakker, Semiclassical theory of shot noise in mesoscopic conductors, *Physica A* **230**, 219 (1996).
- [77] S. Datta, *Electronic Transport in Mesoscopic Systems* (Cambridge University Press, 1995).
- [78] S. Bedkihal, M. Bandyopadhyay, and D. Segal, The probe technique far from equilibrium: Magnetic field symmetries of nonlinear transport, *Eur. Phys. J. B* **86**, 506 (2013).
- [79] Y. Utsumi, O. Entin-Wohlman, A. Aharony, T. Kubo, and Y. Tokura, Fluctuation theorem for heat transport probed by a thermal probe electrode, *Phys. Rev. B* **89**, 205314 (2014).
- [80] See supplementary material for further information.
- [81] P. Roulleau, F. Portier, P. Roche, A. Cavanna, G. Faini, U. Gennser, and D. Mailly, Tuning Decoherence with a Voltage Probe, *Phys. Rev. Lett.* **102**, 236802 (2009).
- [82] H. Haug and A.-P. Jauho, *Quantum Kinetics in Transport and Optics of Semiconductors* (Springer, Berlin, Germany).
- [83] J. P. Bergfield, S. M. Story, R. C. Stafford, and C. A. Stafford, Probing Maxwell's Demon with a Nanoscale Thermometer, *ACS Nano* **7**, 4429 (2013).
- [84] A. Shastry and C. A. Stafford, Temperature and voltage measurement in quantum systems far from equilibrium, *Phys. Rev. B* **94**, 155433 (2016).
- [85] D. Zhang, X. Zheng, and M. Di Ventra, Local temperatures out of equilibrium, *Phys. Rep.* **830**, 1 (2019).
- [86] A. Shastry, S. Inui, and C. A. Stafford, Scanning tunneling thermometry, *Phys. Rev. Appl.* **13**, 024065 (2020).
- [87] L. Tesser, R. S. Whitney, and J. Splettstoesser, Thermodynamic performance of hot-carrier solar cells: A quantum transport model, *Phys. Rev. Appl.* **19**, 044038 (2023).
- [88] A. Braggio, M. Carrega, B. Sothmann, and R. Sánchez, Nonlocal thermoelectric detection of interaction and correlations in edge states, *Phys. Rev. Res.* **6**, L012049 (2024).
- [89] J. R. Prance, C. G. Smith, J. P. Griffiths, S. J. Chorley, D. Anderson, G. A. C. Jones, I. Farrer, and D. A. Ritchie, Electronic refrigeration of a two-dimensional electron gas, *Phys. Rev. Lett.* **102**, 146602 (2009).
- [90] A. A. M. Staring, L. W. Molenkamp, B. W. Alphenaar, H. van Houten, O. J. A. Buyk, M. A. A. Mabeesoone, C. W. J. Beenakker, and C. T. Foxon, Coulomb-Blockade Oscillations in the Thermopower of a Quantum Dot, *EPL* **22**, 57 (1993).
- [91] A. S. Dzurak, C. G. Smith, C. H. W. Barnes, M. Pepper, L. Martín-Moreno, C. T. Liang, D. A. Ritchie, and G. A. C. Jones, Thermoelectric signature of the excitation spectrum of a quantum dot, *Phys. Rev. B* **55**, R10197 (1997).
- [92] N. Nakpathomkun, H. Q. Xu, and H. Linke, Thermoelectric efficiency at maximum power in low-dimensional systems, *Phys. Rev. B* **82**, 235428 (2010).
- [93] S. F. Svensson, A. I. Persson, E. A. Hoffmann, N. Nakpathomkun, H. A. Nilsson, H. Q. Xu, L. Samuelsson, and H. Linke, Lineshape of the thermopower of quantum dots, *New J. Phys.* **14**, 033041 (2012).
- [94] M. Josefsson, A. Svilans, A. M. Burke, E. A. Hoffmann, S. Fahlvik, C. Thelander, M. Leijnse, and H. Linke, A quantum-dot heat engine operating close to the thermodynamic efficiency limits, *Nat. Nanotechnol.* **13**, 920 (2018).
- [95] G. Breit and E. Wigner, Capture of slow neutrons, *Phys. Rev.* **49**, 519 (1936).
- [96] M. Nilsson, L. Namazi, S. Lehmann, M. Leijnse, K. A. Dick, and C. Thelander, Single-electron transport in InAs nanowire quantum dots formed by crystal phase engineering, *Phys. Rev. B* **93**, 195422 (2016).
- [97] D. Barker, S. Lehmann, L. Namazi, M. Nilsson, C. Thelander, K. A. Dick, and V. F. Maisi, Individually addressable double quantum dots formed with nanowire polytypes and identified by epitaxial markers, *Appl. Phys. Lett.* **114**, 183502 (2019).
- [98] A. N. Jordan, B. Sothmann, R. Sánchez, and M. Büttiker, Powerful and efficient energy harvester with resonant-tunneling quantum dots, *Phys. Rev. B* **87**, 075312 (2013).
- [99] B. Szukiewicz, U. Eckern, and K. I. Wysokiński, Optimisation of a three-terminal nonlinear heat nano-engine, *New J. Phys.* **18**, 023050 (2016).
- [100] J. Balduque and R. Sánchez, Coherent control of thermoelectric currents and noise in quantum thermocouples, *Phys. Rev. B* **109**, 045429 (2024).
- [101] I. B. Levinson, Potential distribution in a quantum point contact, *Sov. Phys. JETP* **68**, 1257 (1989); Zh.

- Eksp. Teor. Fiz **95**, 2175 (1989).
- [102] M. Buttiker, Capacitance, admittance, and rectification properties of small conductors, *J. Phys.: Condens. Matter* **5**, 9361 (1993).
- [103] D. Sánchez, R. Sánchez, R. López, and B. Sothmann, Nonlinear chiral refrigerators, *Phys. Rev. B* **99**, 245304 (2019).
- [104] L. P. Kouwenhoven, C. M. Marcus, P. L. McEuen, S. Tarucha, R. M. Westervelt, and N. S. Wingreen, Electron transport in quantum dots, in *Mesoscopic Electron Transport*, edited by L. L. Sohn, L. P. Kouwenhoven, and G. Schön (Springer Netherlands, Dordrecht, 1997) pp. 105–214.
- [105] G. Marchegiani, A. Braggio, and F. Giazotto, Nonlinear thermoelectricity with electron-hole symmetric systems, *Phys. Rev. Lett.* **124**, 106801 (2020).
- [106] G. Germanese, F. Paolucci, G. Marchegiani, A. Braggio, and F. Giazotto, Bipolar thermoelectric Josephson engine, *Nat. Nanotechnol.* **17**, 1084 (2022).
- [107] S. Battisti, G. De Simoni, L. Chirolli, A. Braggio, and F. Giazotto, Bipolar thermoelectric superconducting single-electron transistor, *Phys. Rev. Res.* **6**, L012022 (2024).
-



**SUPPLEMENTARY MATERIAL FOR: “SCATTERING THEORY OF THERMAL AND BIPOLAR THERMOELECTRIC DIODES”**

In this supplementary material we give additional details useful for the discussion in the main text. Section I presents the scattering matrices of the different regions of the conductor and how they lead to the global scattering matrix of the system. Section II gives a derivation of the analytical results demonstrating the rectification induced by a thermalization probe in a minimal model. The model including two resonant tunneling barriers separated by a thermalization probe is analyzed in Secs. III (linear response) and IV. The later includes a discussion of the physical mechanism leading to the bipolar thermoelectric diode, the effect of the coupling to the thermalization probe and the temperature dependence. The physical interpretation and temperature dependence of the screening-induced bipolar diode is given in Sec. V. Finally, we include in Sec. VI plots of the currents and rectification coefficients in different parameter configurations.

## I. SCATTERING MATRICES

### A. Matrix for the coupling to the probe

The coupling to the probe terminal is introduced by the scattering matrix [60]:

$$\mathcal{S}^\lambda = \begin{pmatrix} 0 & \sqrt{1-\lambda} & 0 & i\sqrt{\lambda} \\ \sqrt{1-\lambda} & 0 & i\sqrt{\lambda} & 0 \\ i\sqrt{\lambda} & 0 & \sqrt{1-\lambda} & 0 \\ 0 & i\sqrt{\lambda} & 0 & \sqrt{1-\lambda} \end{pmatrix}, \quad (\text{S1})$$

where  $\lambda$  is the probability of an electron in region 2 to be absorbed and thermalized by the probe. In the matrix, indices 1 and 2 correspond to the conductor channels connecting to regions 1 and 3; indices 3 and 4 correspond to channels connected to the probe terminal. Note that  $\lambda$  is treated in the same footing as other transmission probabilities in the scattering region.

In the configuration considered in the main text, for  $\lambda = 0$ , transport between the other conductor terminals (L and R) is elastic. For  $\lambda = 1$ , all electrons are thermalized to the probe distribution when entering the central region. Transport can in that case be understood in terms of scattering between three thermal reservoirs (L, R and the probe) separated by regions 1 and 3.

### B. Resonant tunneling barriers

In a mesoscopic conductor, resonant tunneling appears typically in double-barrier structures forming quantum dots or quantum wells. Considering symmetric barriers

and a single resonant state, the single-channel scattering can be described by a Breit-Wigner [95] scattering matrix

$$\mathcal{S}^{\text{RTB}} = \begin{pmatrix} 1 + \tau & \tau \\ \tau & 1 + \tau \end{pmatrix}, \quad (\text{S2})$$

with transmission amplitude

$$\tau = \frac{-i\Gamma}{E - \varepsilon + i\Gamma}, \quad (\text{S3})$$

where  $\varepsilon$  is the energy of the resonant state and  $\Gamma/\hbar$  is its inverse lifetime due to coupling to the modes outside the double barrier [60].

### C. Scattering matrix for the total system

When the transport is fully elastic in the system the total scattering matrix have to account for processes that involve both scattering regions  $\mathcal{S}_1$ ,  $\mathcal{S}_3$ , and the possible coherent reflections between them, where electrons accumulate a kinetic phase  $k(E)d$ ; with  $k(E) = \sqrt{2m(E - U_2)}$  the electron wavenumber in region 2. This is done by taking into account that e.g., the right-outgoing wave from region 1 is the left-ingoing wave at region 3, multiplied by a phase factor  $e^{ik(E)d}$ , and solving for all the outgoing waves as functions of the ingoing ones [34, 77]. Defining  $E_\alpha = E - U_\alpha$ , the total scattering matrix reads:

$$\begin{aligned} \mathcal{S}(E, \mathbf{U}) &= \begin{pmatrix} r(E, \mathbf{U}) & \tau(E, \mathbf{U}) \\ \tau(E, \mathbf{U}) & r'(E, \mathbf{U}) \end{pmatrix}, \\ \tau(E, \mathbf{U}) &= \frac{e^{ik(E)d}\Gamma^2}{e^{ik(E)d/l_0}E_1E_3 + (E_1 - i\Gamma)(E_3 - i\Gamma)} \\ r(E, \mathbf{U}) &= \frac{E_1(E_3 - i\Gamma) - e^{ik(E)d}E_3(E_1 - i\Gamma)}{e^{ik(E)d}E_1E_3 + (E_1 - i\Gamma)(E_3 - i\Gamma)} \\ r'(E, \mathbf{U}) &= \frac{E_3(E_1 - i\Gamma) - e^{ik(E)d}E_1(E_3 - i\Gamma)}{e^{ik(E)d}E_1E_3 + (E_1 - i\Gamma)(E_3 - i\Gamma)}. \end{aligned} \quad (\text{S4})$$

One should be careful when using the scattering matrix obtained by this approach to calculate injectivities for energies below  $\mathbf{U}$ , as it gives spurious divergences near the band bottom that are not present when using exact wave-function matching methods. This is relevant for the determination of the excess injected charge, as it involve the calculation of an integral starting from the energy origin. Here we have dealt numerically with this issue.

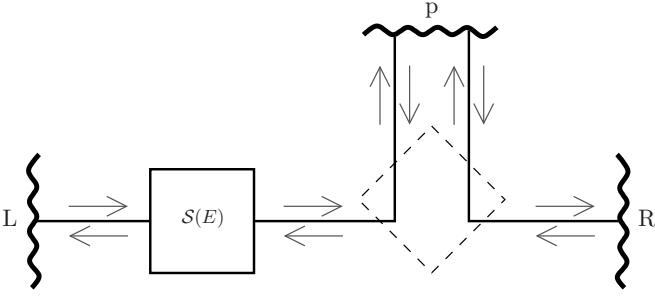


FIG. S1. Minimal configuration showing rectification by thermalization with a fully transparent coupling ( $\lambda = 1$ ) to a probe terminal, p. A barrier represented by the scattering matrix  $S$  is placed between terminal L and the probe.

## II. MINIMAL MODEL WITH THERMALIZATION

Consider the situation depicted in Fig. S1, with a fully transparently coupled ( $\lambda = 1$ ) thermalization probe terminal, p, and a scattering region connecting it with terminal L with a transmission probability  $\mathcal{T}(E) = |\mathcal{S}_{Lp}(E)|^2$ . Electrons injected from terminal R are all absorbed by the probe. We impose  $\mu_L = \mu_R = \mu$  to the conductor terminals and  $I_p = J_p = 0$  to the probe.

The conductor currents are given by

$$I_L = \frac{2}{h} \int dE \mathcal{T}(E) (f_L - f_p) \quad (\text{S5})$$

$$I_R = \frac{2}{h} \int dE (f_R - f_p) = \frac{2}{h} (\mu - \mu_p), \quad (\text{S6})$$

for particles and

$$J_L = \frac{2}{h} \int dE (E - \mu) \mathcal{T}(E) (f_L - f_p) \quad (\text{S7})$$

$$J_R = \frac{2}{h} \int dE (E - \mu) (f_R - f_p) = \frac{\pi^2}{3h} (T_R^2 - T_p^2), \quad (\text{S8})$$

for heat. In the probe,  $I_p = -I_L - I_R$  and  $J_p = -J_L - J_R$ . With charge and energy conservation, the current through the conductor is fully determined by the exact expressions for  $I_R$  and  $J_R$  above given by  $\mu - \mu_p$  and  $T_R^2 - T_p^2$ . In order to have a diode effect, such that  $I_L^F \neq I_L^B$  and  $J_L^F \neq J_L^B$ , it is hence enough to prove that  $\mu_p^F \neq \mu_p^B$  and  $T_p^F \neq T_p^B$ , respectively.

For the thermoelectric case, it is easy to show that if  $\mathcal{T}$  is energy independent, so it induces no thermoelectric effect in the probe, we get  $I_L = 2\mathcal{T}(\mu - \mu_p)/h$  independently of the temperature  $T_L$ . Therefore, the only current-conserving solution is  $\mu_p = \mu$ , indeed giving  $I^F = I^B = 0$ . If we now consider an energy-dependent transmission probability,

$$I_L^F = \frac{2}{h} \int dE \mathcal{T}(E) [f(T + \Delta T) - f_p] \quad (\text{S9})$$

and

$$I_L^B = \frac{2}{h} \int dE \mathcal{T}(E) [f(T) - f_p] \quad (\text{S10})$$

are necessarily different, as long as the scatterer breaks electron-hole symmetry i.e., if it has a finite thermoelectric response. In that case, from Eq. (S6) we get  $\mu_p^F \neq \mu_p^B$ .

For the heat currents, it is sufficient to assume that  $0 < \mathcal{T} < 1$ . In the simplest case where it is energy independent, we get

$$J_L^F = \frac{\mathcal{T}\pi^2}{3h} [(T + \Delta T)^2 - (T_p^F)^2] = \frac{\pi^2}{3h} [T^2 - (T_p^F)^2]$$

$$J_L^B = \frac{\mathcal{T}\pi^2}{3h} [T^2 - (T_p^B)^2] = \frac{\pi^2}{3h} [(T + \Delta T)^2 - (T_p^B)^2]. \quad (\text{S11})$$

Solving for the probe temperatures, we get:

$$(T_p^F)^2 = (\mathcal{T} - 1)T^2 + \mathcal{T}(\Delta T^2 + 2T\Delta T) \quad (\text{S12})$$

$$(T_p^B)^2 = (\mathcal{T} - 1)T^2 - \mathcal{T}(\Delta T^2 + 2T\Delta T), \quad (\text{S13})$$

clearly showing a diode effect,  $T_p^F \neq T_p^B$ .

## III. LINEAR RESPONSE OF A THERMALIZATION PROBE

Consider two scattering regions,  $\alpha = 1, 3$  separated by a transparently coupled probe terminal, such that all electrons injected from terminals L and R are either reflected at the barriers or absorbed by the probe. The electrochemical potential,  $\mu_p$ , and temperature,  $T_p$ , of the probe need to be calculated to fulfill the conditions  $I_p = J_p = 0$ . Current is only due to a temperature difference  $\Delta T$  applied to terminal L in the forward (F), or to R in the backward configuration (B). Let us consider first the forward case, where we expand the particle and heat currents as:

$$I_L^F = -G_1 \Delta \mu_p^F + L_1 (\Delta T - \Delta T_p^F) \quad (\text{S14})$$

$$I_R^F = -G_3 \Delta \mu_p^F - L_3 \Delta T_p^F \quad (\text{S15})$$

$$J_L^F = -M_1 \Delta \mu_p^F + K_1 (\Delta T - \Delta T_p^F) \quad (\text{S16})$$

$$J_R^F = -M_3 \Delta \mu_p^F - K_3 \Delta T_p^F, \quad (\text{S17})$$

where  $\Delta \mu_p^F = \mu_p^F - \mu$  and  $\Delta T_p^F = T_p^F - T$ .  $G_\alpha$ ,  $L_\alpha$ ,  $M_\alpha$  and  $K_\alpha$  are the electrical conductance, Seebeck coefficient, Peltier coefficient and thermal conductance of scattering region  $\alpha$ , respectively. Solving for the probe conditions, we get:

$$\Delta \mu_p^F = \frac{L_1 K_3 - L_3 K_1}{G_\Sigma K_\Sigma - L_\Sigma M_\Sigma} \Delta T$$

$$\Delta T_p^F = \frac{G_\Sigma K_1 - L_1 M_\Sigma}{G_\Sigma K_\Sigma - L_\Sigma M_\Sigma} \Delta T, \quad (\text{S18})$$

where the subindex  $\Sigma$  indicates the sum over L and R. With these, we get the currents:

$$\begin{aligned} I_L^F &= \frac{G_1 L_3 K_1 + G_3 L_1 K_3 - L_1 L_3 M_\Sigma}{G_\Sigma K_\Sigma - L_\Sigma M_\Sigma} \Delta T \\ J_L^F &= \frac{K_1 K_3 G_\Sigma - K_1 L_3 M_3 - K_3 L_1 M_1}{G_\Sigma K_\Sigma - L_\Sigma M_\Sigma} \Delta T. \end{aligned} \quad (\text{S19})$$

For the backward currents, we simply replace  $1 \leftrightarrow 3$  in Eqs. (S18) and (S19). This way we obtain

$$\Delta\mu_p^F = -\Delta\mu^B, \quad (\text{S20})$$

as well as  $I_L^F = -I_L^B$  and  $J_L^F = -J_L^B$ . As expected, there is no rectification in the linear regime.

### A. Antisymmetric configuration

A particularly interesting case is when the transmission of region 3,  $\mathcal{T}_3(E)$  is the reflection of  $\mathcal{T}_1(E)$  over the electrochemical potential. Then,  $G_1 = G_3$ ,  $L_1 = -L_3$ ,  $M_1 = -M_3$  and  $K_1 = K_3$ . In that case, we get:

$$\Delta\mu_p^F = \frac{L_1}{2G_1} \Delta T \quad \text{and} \quad \Delta T_p^F = \frac{\Delta T}{2}, \quad (\text{S21})$$

and

$$I_L^F = 0 \quad \text{and} \quad J_L^F = \frac{K}{2} \Delta T. \quad (\text{S22})$$

In the same way,  $I_L^B = 0$ . Therefore in this case only the nonlinear contributions are responsible for the thermoelectric particle currents.

## IV. BIPOLAR DIODE BY THERMALIZATION

The thermalization-induced bipolar thermoelectric diode occurs around the condition when the resonances of scatterers 1 and 3 are antisymmetric with respect to the base electrochemical potential,  $\mu$ , and have a similar (but opposite) response to electrochemical and temperature differences with the probe terminal. That is the case represented in Fig. S2. In order to understand this effect, it is important to first notice that the temperature difference is the only thermodynamic force. Hence, the flow of heat is well defined by the second law of thermodynamics (and by everyone's intuition) and goes from the hot to the cold reservoir, i.e., it has opposite sign in the forward and the backward configurations. Differently, the sign of the thermoelectric current is not fixed by any thermodynamic law. In this particular case, it depends on the developed potential in the probe.

Consider first the forward configuration, cf. Fig. S2(a), in which the thermalization probe initially has an electrochemical potential  $\mu$  but its temperature is already the one fixed by the probe conditions  $I_p = J_p = 0$ . Clearly,  $T_R < T_p < T_L$ , see Fig. S2(c). For concreteness, we fix

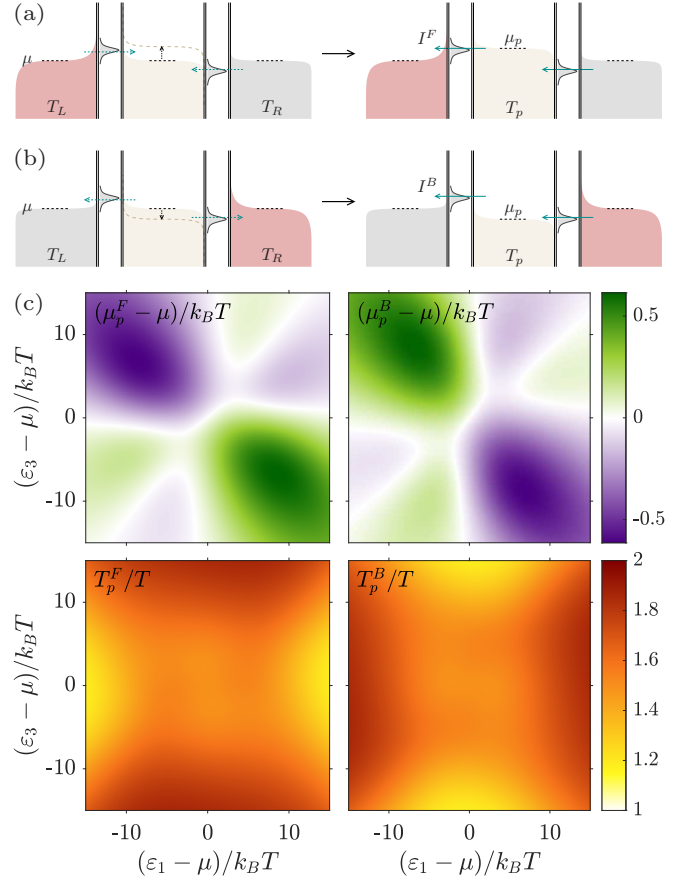


FIG. S2. Mechanism for bipolar rectification induced by the thermalization probe. The two panels show how the contributions to the particle flows through the two barriers change with the chemical potential developed at the probe in (a) the forward and (b) the backward configurations. The left column shows the sign of the (purely) thermoelectric contributions when  $\mu_p = \mu$ . In the right column, these contributions have modified  $\mu_p$ , resulting in the reversal of the flows through one of the barriers. (c) Electrochemical potential and temperature developed at the thermalization probe in the forward and backward configurations. Parameters:  $\Gamma = 3k_B T$ ,  $\mu = 40k_B T$ , and  $\Delta T/T = 1$ .

$\varepsilon_1 = -\varepsilon_3 > \mu$ . In such a situation, the thermoelectric response of the two resonant tunneling barriers results in charge flowing into the conductor: particles flow from the hotter to the colder reservoir when the resonance is over the electrochemical potential, and in the opposite direction when it is below [53]. The probe terminal hence increases its electrochemical potential, as shown in Fig. S2(c). The voltage established between terminals L and R and the probe introduces another contribution to the particle current (additional to the temperature-driven thermoelectric response). In this particular configuration, the distance  $\varepsilon_1 - \mu_p$  is reduced, while  $\varepsilon_3 - \mu_p$  increases, so transport through barrier 1 is most sensitive to this change. Eventually (when  $\mu_p - \mu$  attains the thermovoltage of barrier 1 under a temperature dif-

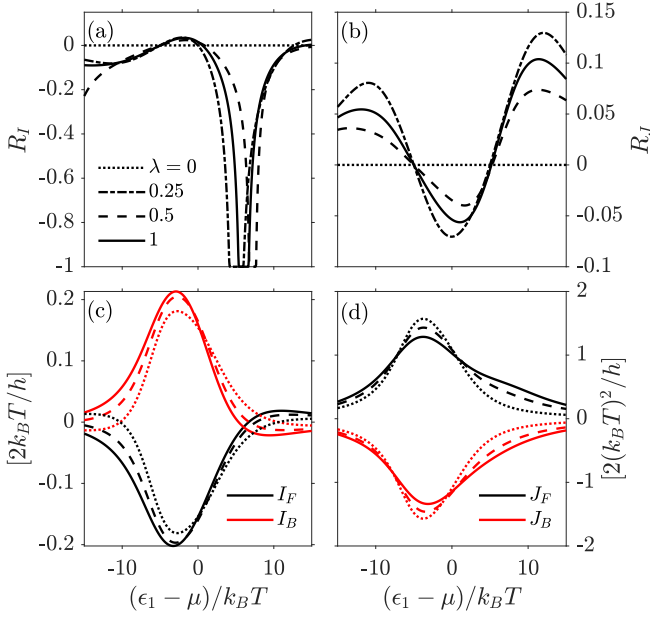


FIG. S3. Effect of the coupling to the thermalization probe on (a) the thermoelectric and (b) thermal rectification coefficients. (c) and (d) show the corresponding particle and heat currents. Parameters:  $\Gamma = 3k_B T$ ,  $\mu = 40k_B T$ ,  $\Delta T = T$ ,  $d = 2h/\sqrt{8mk_B T}$  and  $(\epsilon_3 - \mu) = -5k_B T$ .

ference  $T_L - T_p$ ), the voltage-induced contribution developed by thermalization is able to reverse the flow of particles through barrier 1. The particle current through the conductor then flows from R to L and  $I^F < 0$ .

In the backward configuration, see Fig. S2(b), the same arguments apply, with the difference that, as the resonances are opposite, when exchanging the temperatures  $T_L$  and  $T_R$ , the initial thermoelectric contributions have the opposite sign, i.e., the flow into the  $L$  and  $R$  terminals. Then, the electrochemical potential of the probe tends to diminish, see Fig. S2(c), again approaching the resonance coupled to the hot reservoir ( $\epsilon_3$ ), so it is the contribution through barrier 3 the one that is finally reversed. As a consequence, we again have particles flowing from  $R$  to  $L$ , i.e.,  $I^B < 0$ .

In the perfectly antisymmetric case, we furthermore have  $I^F = I^B < 0$ .

### A. Effect of the finite coupling to the probe

In the main text we have discussed the case where all the electrons entering the center region are thermalized by the probe, with  $\lambda = 1$ . The effect of a finite coupling to the probe is plotted in Fig. S3, showing that the rectification coefficients and currents have the same qualitative behaviour. In particular, the bipolar thermoelectric effect is robust to finite  $\lambda$ , though the region where it appears is reduced with the opacity of the coupling.

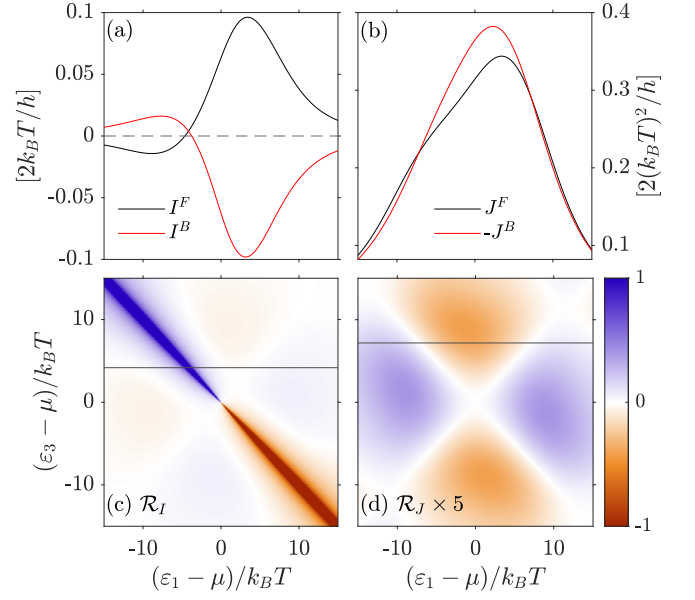


FIG. S4. Thermalization diode. Forward and backward (a) particle and (b) heat currents as functions of  $\epsilon_1$  tuned along  $(\epsilon_3 - \mu)/k_B T = 4.8$  and  $8.7$ , respectively, indicated by black lines in (c) and (d), correspondingly. The later panels show the thermoelectric and heat rectification coefficients, as functions of both resonances. The thermalization probe is fully coupled ( $\lambda = 1$ ), and  $\mu \gg U_\alpha$ , so the band bottom has no effect. Parameters:  $\Gamma = 3k_B T$ ,  $\mu = 40k_B T$ , and  $\Delta T/T = 1/2$ .

### B. Temperature dependence

We plot in Fig. S4 the currents and rectification coefficient for  $\Delta T = T/2$ , showing that, though expectedly weaker, the same effects discussed in the main text for  $\Delta T = T$  also appear in this case. Antireciprocal thermoelectric currents are restricted to a narrower region around  $\epsilon_1 = -\epsilon_3$ . This is because the shift of  $\mu_2$  is not large enough to invert one of the currents far from the antisymmetric condition.

Figure S5 shows the temperature dependence of the thermalization-induced bipolar thermoelectric and thermal diode effects for two configurations of Fig. 3 of the main text. The one for the thermoelectric case is chosen slightly de-tuned from the antisymmetric configuration with  $\epsilon_1 + \epsilon_3 = 0$ , for which we find  $\mathcal{R}_I = 1$  for every  $\Delta T, T$ . In this particular configuration, the bipolar thermoelectric diode still occurs for almost all temperature configurations, see Figs. S5(a) and S5(c). Only close to the linear response regime, with small temperature differences, we have  $\mathcal{R}_I < 1$ . As shown in Figs. S5(b) and S5(d), the difference of the forward and backward currents increases with  $\Delta T$ , as expected. The thermal rectification coefficient however saturates. We have introduced a new reference temperature  $T_0$  specifically for this plot.

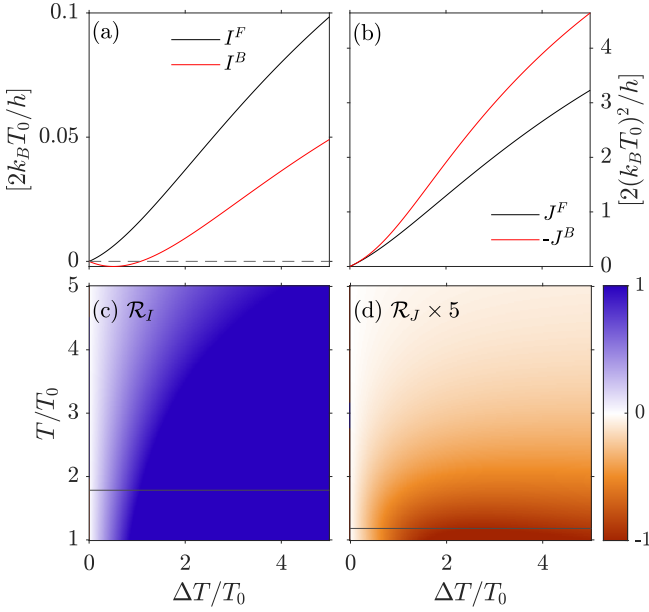


FIG. S5. Temperature dependence of the thermalization-induced rectification. Forward and backward (a) particle and (b) heat currents as functions of  $\Delta T$  for temperatures  $T = 1.8T_0$  and  $1.2T_0$ , respectively, indicated by black lines in (c) and (d), correspondingly. The later panels show the thermoelectric and heat rectification coefficients, as functions of  $\Delta T/T_0$  and  $T/T_0$ , for configurations of Fig. 3 of the main text with  $(\epsilon_1 - \mu)/k_B T_0 = -6$  and  $0$ , and  $(\epsilon_1 - \mu)/k_B T_0 = 7$  and  $10$  respectively. The remaining parameters are the same, with  $\lambda = 1$ .

### V. BIPOLAR DIODE BY SCREENING EFFECTS

The screening-induced bipolar thermoelectric diode occurs when the transmission energy dependence presents two nonzero contributions, one above and one below the reference electrochemical potential, as sketched in Fig. S6 and plotted in Fig. S7(a): a wide double-peak at positive energies, due to the two Breit-Wigner resonances being close in energy, and a sharp peak at negative energies, due to the Fabry-Perot interference in region 2. The nonlinear response will depend on how the internal energies  $U_\alpha$  react to the temperature increase in one of the reservoirs, therefore modifying the overall transmission probability,  $\mathcal{T}(\{\mathbf{U}\})$ . The internal energies are obtained self-consistently by solving the change in the induced charge,  $\delta q_\alpha$ , in each region. This is given by the injectivities  $\nu_{j\alpha}$  from terminal  $j$  into region  $\alpha$  via

$$\frac{\delta q_\alpha}{-e} = \int dE \sum_j [\nu_{j\alpha}(E, \mathbf{U}) f_j(E) - \nu_{j\alpha}^{\text{eq}} f_{\text{eq}}(E)], \quad (\text{S23})$$

see main text. Clearly for a given region the injectivity is larger for the terminal with which it is directly coupled i.e.,  $\nu_{L1} \gg \nu_{R1}$  and  $\nu_{R3} \gg \nu_{L3}$ , see Figs. S7(b) and S7(c). Hence, one expects the potential of region 1(3)

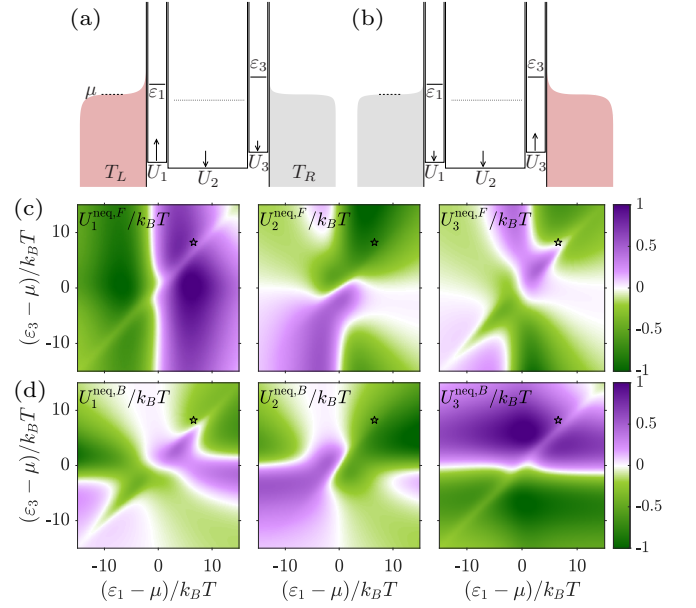


FIG. S6. Scheme of the developed internal potentials,  $U_\alpha$ , induced by charge accumulation in (a) the forward and (b) the backward configurations. Solid lines mark the energy of the resonances,  $\epsilon_1 < \epsilon_3$ , with the dotted line indicating the position of a Fabry-Perot interference peak. Under the appropriate conditions, this effect results in a bipolar thermoelectric diode with particles flowing from  $L$  to  $R$  in both configurations. Developed nonequilibrium electrostatic energies in the three regions for the (c) forward and (d) backward configurations. Same configuration as in Fig. 3 in the main text, with  $\lambda = 0$ ,  $d = 2h/\sqrt{8mk_B T}$ ,  $\Gamma = 1k_B T$ ,  $\mu = 40k_B T$  and  $\Delta T = T$ .

to change more in the forward (backward) configuration. The opposite region in each configuration is expected to be barely affected by the temperature increase, therefore this small modification can then also be influenced by the charging of the other regions via the self-consistency.

To get a better intuition, let us focus on a particular configuration, as the one sketched in Fig. S6, with both Breit-Wigner resonances having energies over the chemical potential,  $\mu < \epsilon_1 < \epsilon_3$ . Close to equilibrium (for small temperature differences), the current is dominated by the Breit-Wigner resonances, so particles flow from  $L$  to  $R$  in the forward, and opposite in the backward configuration. Consider first the forward configuration, depicted in Fig. S6(a). The change in the nonequilibrium electrostatic energies is shown in Fig. S6(c) as the resonances are tuned. The temperature increase in terminal  $L$  contributes to charge region 1 by increasing the occupation of the lead at the energies around  $\epsilon_1$  (for enhancing the tail of the Fermi distribution). Hence,  $U_1$  is expected to increase. The next region to consider is region 2, whose coupling to terminal  $L$  is weaker. This region features a sharp interference peak below the chemical potential, thus resulting on a decrease of the charge with respect to the equilibrium state (states of the lead below the chemical potential are less occupied when increasing

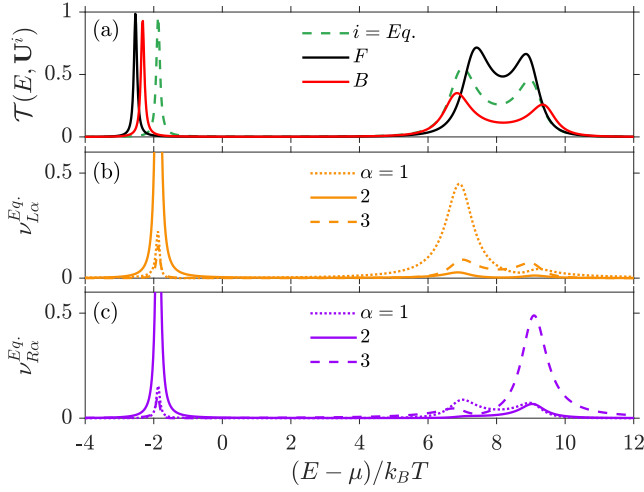


FIG. S7. (a) Transmission probability when the system is in equilibrium (solid green), and in the forward (dashed black) and backward (dotted red) configurations, once the electrostatic potentials have build-up in the three areas as a result of the corresponding non-equilibrium situation. (b)-(c) In-junctivities in regions  $\alpha = 1, 2, 3$  from reservoirs  $L$  and  $R$ , respectively. The parameters correspond to the ones where  $I^B = I^F \neq 0$  in Fig. 3(e) of the main text, marked by  $\star$  in Fig. 3(a) [as well in Fig. S6(c) and S6(d)].

the terminal temperature), so  $U_2$  decreases. Finally, region 3 is in this case little affected by the temperature variation in terminal L, but it can be indirectly affected by the potential variation in the regions in between: the change in  $U_1$  and  $U_2$  also affects region 3 and compete in the resulting  $U_3$  is a complicated manner. In this particular case, it also decreases. With this, the two Breit-Wigner resonances in regions 1 and 3 are then brought closer in energy, resulting in a narrower and sharper feature at positive energies in the transmission probability, see Fig. S7(a), which is favorable for the thermoelectric current from L to R.

The same arguments apply to the backward configuration, depicted in Fig. S6(b). The developed  $U_\alpha^{\text{neq}}$  are shown in Fig. S6(d). In this case, it results in  $U_1$  decreasing and  $U_3$  increasing, which separates the two Breit-Wigner resonances and makes the double peak at positive energies wider and lower, see Fig. S7(a). Thus the thermoelectric contribution at positive energies (from the hot R to the cold L) is reduced. The Fabry-Perot interference peak, being at negative energies contributes to transport in the opposite direction (from L to R). Eventually, the Breit-Wigner contribution gets so weak that the Fabry-Perot contribution, which is robust to the change in temperature, starts to dominate. At that point, the current through the system changes sign, so particles flow from L to R, as in the forward configuration.

In other words, the antireciprocal effect is due to a change of the contribution of positive- and negative-energy spectral features, which contribute oppositely to the thermoelectric response.

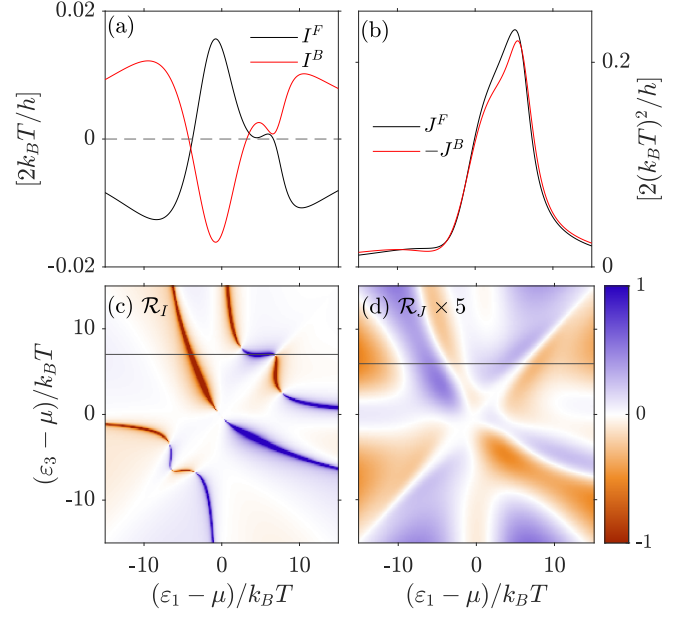


FIG. S8. Rectification by screening. Forward and backward (a) particle and (b) heat currents as functions of  $\varepsilon_1$ , for fixed  $(\varepsilon_3 - \mu)/k_B T = 8.2$  and  $7.5$  as marked by black lines in (c) and (d), respectively. The later show the dependence of  $\mathcal{R}_I$  and  $\mathcal{R}_J$  with gating the RTBs. Parameters:  $\lambda=0$ ,  $d = 2h/\sqrt{8mk_B T}$ ,  $\Gamma = k_B T$ ,  $\mu = 40k_B T$ ,  $\Delta T/T = 1/2$ .

### A. Temperature dependence

Figure S8 shows the thermoelectric and thermal rectification properties at a lower temperature difference than the one considered in the main text,  $\Delta T = T/2$ . The same features observed in Fig. 3 of the main text appear, with smaller rectification coefficients, as expected. The bipolar thermoelectric diode occurs in narrower regions of the gate-voltage map.

The temperature dependence is plotted in Fig. S9 for the particular gating corresponding to Fig. S7 (marked with a  $\star$  in Fig. 3(a) of the main text). It shows that the bipolar thermoelectric diode occurs for wide temperature ranges, cf. Figs. S9(a) and S9(c), showing a threshold at low temperatures and temperature gradients which is tunable with gating. The thermal currents show a robust diode effect, with the  $I^F$  increasing with  $\Delta T$ , while  $I^B$  saturates and even shows negative thermal differential conductance for large enough  $\Delta T$ , cf. Fig. S9(b). The thermal rectification coefficient increases both with  $T$  and  $\Delta T$ , see Fig. S9(d).

## VI. CHARGE AND HEAT CURRENTS

Figures S10, S11, S12 and S13 show the forward and backward particle and heat currents as well as the thermoelectric and thermal rectification coefficients for the different configurations as functions of the quantum dot

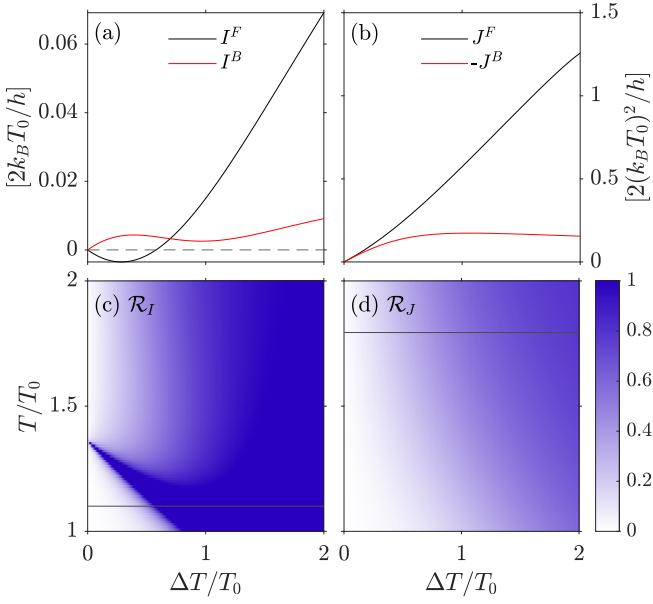


FIG. S9. Temperature dependence of the screening induced rectification. Forward and backward (a) particle and (b) heat currents as functions of  $\Delta T$  for temperatures  $T = 1.1T_0$  and  $1.8T_0$ , respectively, indicated by black lines in (c) and (d), correspondingly. The later panels show the thermoelectric and heat rectification coefficients, as functions of  $\Delta T/T_0$  and  $T/T_0$ . The remaining parameters correspond to the ones where  $I_B = I_F \neq 0$  in Fig. 3(e) of the main text, marked by  $\star$  in Fig. 3(a) [as well in Fig. S6(c) and S6(d)].

linewidth,  $\Gamma$ , and of the distance between barriers 1 and 3,  $d$  (for the thermalization free case with  $\lambda = 0$ , Fig. S12). The thermoelectric currents reach values of the order of nA at  $T = 1$  K and  $\Delta T/T = 1$ , where a bidimensional GaAs device would have a carrier concentration of  $\sim 10^{12}$  cm $^{-2}$  and sizes of tens of nm for the explored regimes.

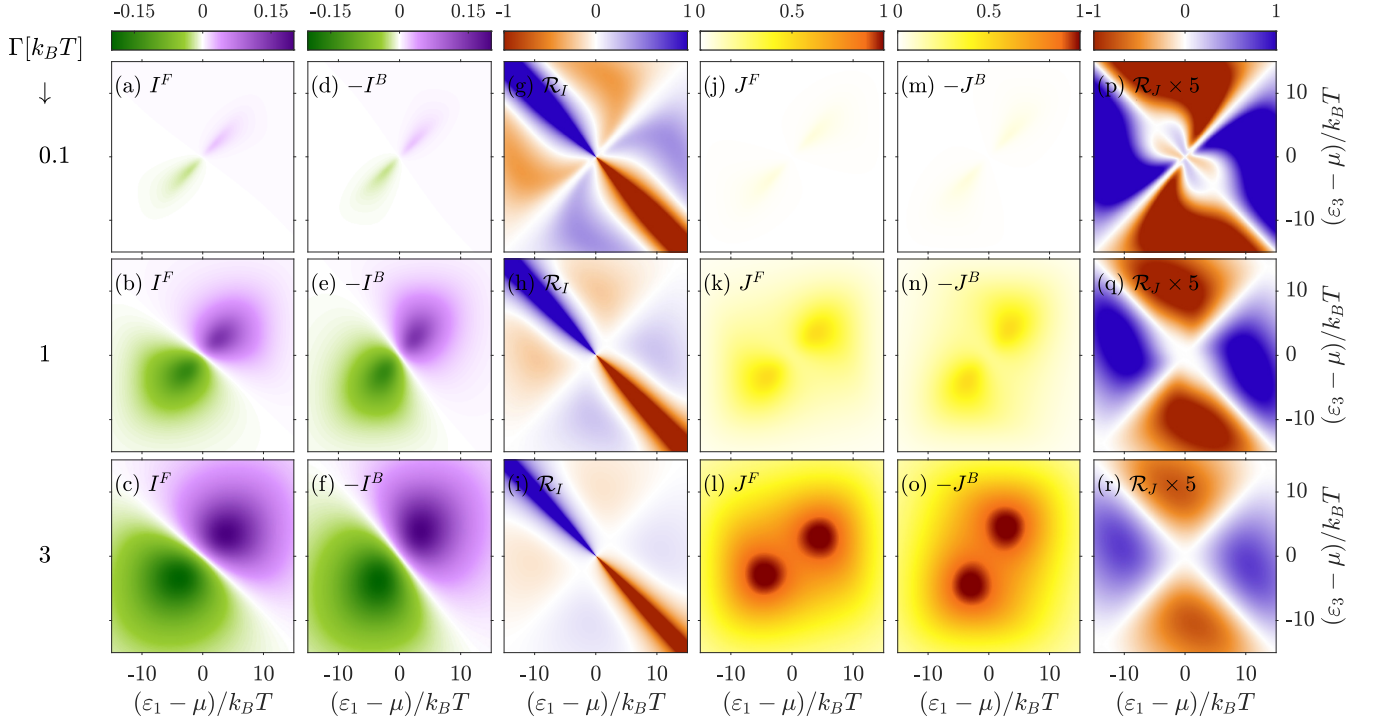


FIG. S10. (a)-(c) Forward and (d)-(f) backward particle currents, and (g)-(i) thermoelectric rectification for the double resonant tunneling barrier conductor sandwiching a strong thermalization region ( $\lambda = 1$ ) and neglecting screening, as functions of the resonance energies,  $\varepsilon_1$  and  $\varepsilon_3$  and for increasing quantum dot linewidth,  $\Gamma$ . (j)-(l), (m)-(o) and (p)-(r) show the corresponding the heat quantities. In all cases,  $\Delta T = T$ .

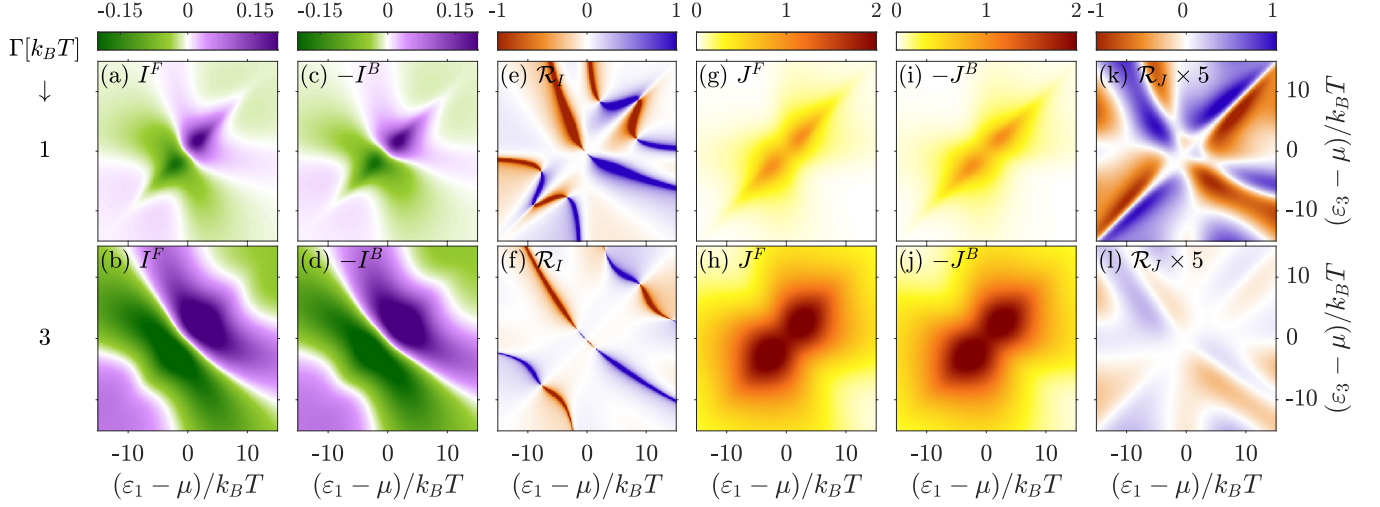


FIG. S11. Same as Fig. S10 in the elastic case with  $\lambda = 0$  including screening effects, for  $d = 2\hbar/\sqrt{8mk_B T}$  and  $\mu = 40k_B T$ .



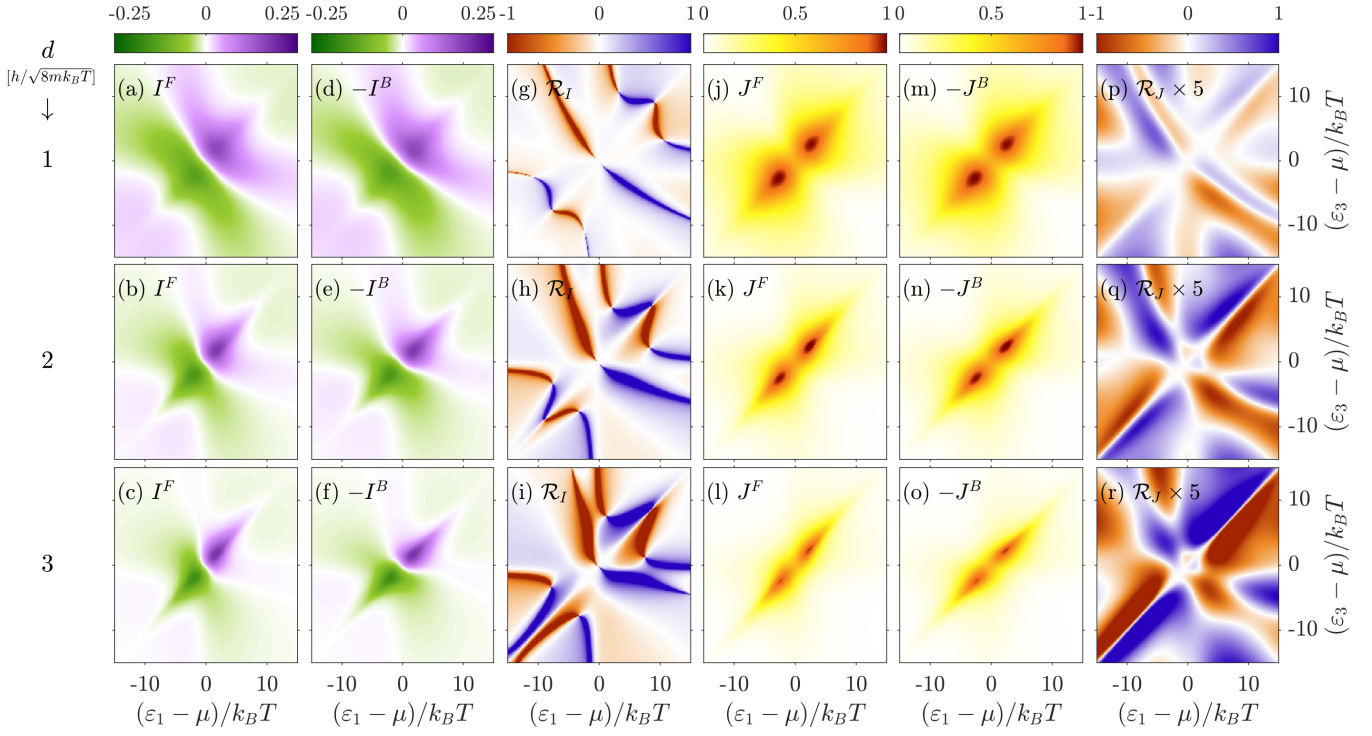


FIG. S12. Same as Fig. S11 for  $\Gamma = k_B T$  and for different lengths of region 2,  $d$ , which controls the position and width of the Fabry-Perot resonance at energies below the chemical potential.

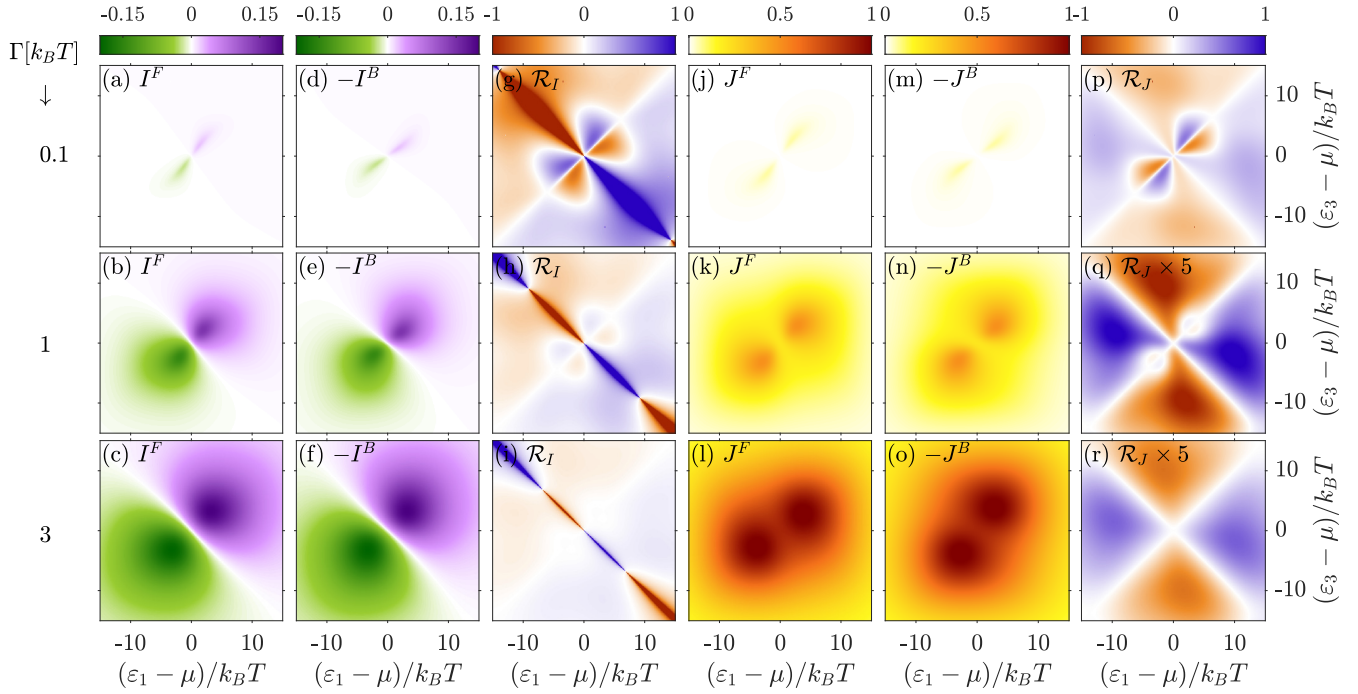


FIG. S13. Same as Fig. S11 in the strong thermalization regime with  $\lambda = 1$ .